APPLIED SCIENCES AND ENGINEERING

Fully implantable wireless batteryless vascular electronics with printed soft sensors for multiplex sensing of hemodynamics

Robert Herbert[1,2], Hyo-Ryoung Lim[3], Bruno Rigo[2,4], Woon-Hong Yeo[1,2,5,6]*

The continuous monitoring of hemodynamics attainable with wireless implantable devices would improve the treatment of vascular diseases. However, demanding requirements of size, wireless operation, and compatibility with endovascular procedures have limited the development of vascular electronics. Here, we report an implantable, wireless vascular electronic system, consisting of a multimaterial inductive stent and printed soft sensors capable of real-time monitoring of arterial pressure, pulse rate, and flow without batteries or circuits. Developments in stent design achieve an enhanced wireless platform while matching conventional stent mechanics. The fully printed pressure sensors demonstrate fast response times, high durability, and sensing at small bending radii. The device is monitored via inductive coupling at communication distances notably larger than prior vascular sensors. The wireless electronic system is validated in artery models, while minimally invasive catheter implantation is demonstrated in an in vivo rabbit study. Overall, the vascular system offers an adaptable framework for comprehensive monitoring of hemodynamics.

INTRODUCTION

Vascular diseases are the leading cause of death, accounting for more than 30% of deaths worldwide (*1*). Diseases and conditions, such as hypertension, atherosclerosis, and aneurysms, occur throughout the vascular system, including in arteries from a few millimeters to centimeters in diameter with varying curvature (*2*). Blood pressures and flow rates, among other hemodynamics, are monitored to follow disease progression and treatment (*3*–*6*). However, current hemodynamic monitoring methods, including angiography, magnetic resonance imaging, Doppler ultrasound, and catheterization, provide narrow and incomplete views of vascular health due to limited and repetitive monitoring periods and patient immobilization (*3*, *6*, *7*). Although continuous hemodynamic monitoring has been shown to improve patient outcomes, existing clinical devices offer limited sensing capabilities due to their bulky packages and rigid materials (*8*–*12*). These devices are suitable for only pressure monitoring within the heart, abdominal aneurysms, and pulmonary artery and are incompatible with other arteries (*9*–*12*). Overall, the development of vascular electronics for arterial sensing has been limited by strict requirements for implantation and operation, including offering sufficient wireless capabilities with a flexible, miniaturized, and low-profile system that affixes itself within an artery and is compatible with minimally invasive catheter implantation. Advances in stretchable and flexible electronics offer a means of forming wireless arterial sensors (*13*–*19*). One recent work targeted vessel anastomosis and demonstrated a cuff-type, flexible pulse sensor that is sutured outside of an artery with a wireless antenna extending outward (*17*). For catheter compatibility, works have developed stent-based systems because stents provide an implantable backbone and are commonly used, with more than 3 million implanted in cardiovascular arteries each year (*19*, *20*). Stent-based systems have attached wireless sensors to stents and have used stents as wireless antennas (*19*, *21*–*23*). However, all existing devices have shortcomings in requiring memory modules, displaying low wireless distances or showing fragility during implantation (*21*–*25*).

This paper reports a vascular electronic system consisting of a wireless stent platform integrated with soft sensors to meet implantation and operation requirements. The device is wirelessly operated by inductive coupling to offer real-time, simultaneous monitoring of pressure, pulse rate, and flow, which offers an opportunity to detect a wide range of vascular conditions. A laser-machining process is developed to form a multimaterial inductive stent, which addresses the key challenge of enabling wireless connectivity while maintaining critical stent mechanics. The soft pressure sensors are fully aerosol jet–printed and conformally integrated with the stent. The use of a printed elastomer pattern as the dielectric enables fast response times and pressure sensing even when bending at a radius of 0.25 mm, which is a key advancement as flexible pressure sensors often are not demonstrated to sense during bending or degrade at bending radii as large as tens of millimeters. The wireless device is compatible with conventional stenting procedures and exhibits a 5.5- and 3.5-cm readout distance in air and blood, which is two to three times improvement in the wireless distance over existing stent-based devices. Device performance is evaluated in a biomimetic silicone artery with pulsatile flow. An in vivo study in a rabbit model demonstrates minimally invasive catheter implantation in an iliac artery with carotid access.

RESULTS

Design and sensing scheme of a wireless vascular electronic system with printed sensors for wireless monitoring of hemodynamics

The implantable wireless device consists of an inductive smart stent integrated with soft, capacitive sensors (Fig. 1A). The stent platform

[1]George W. Woodruff School of Mechanical Engineering, Georgia Institute of Technology, Atlanta, GA 30332, USA. [2]IEN Center for Human-Centric Interfaces and Engineering at the Institute for Electronics and Nanotechnology, Georgia Institute of Technology, Atlanta, GA 30332, USA. [3]Major of Human Biocovergence, Division of Smart Healthcare, College of Information Technology and Convergence, Pukyong National University, Busan, 48513, Republic of Korea. [4]School of Electrical and Computer Engineering, Georgia Institute of Technology, Atlanta, GA 30332, USA. [5]Wallace H. Coulter Department of Biomedical Engineering, Georgia Institute of Technology and Emory University, Atlanta, GA 30332, USA. [6]Parker H. Petit Institute for Bioengineering and Biosciences, Neural Engineering Center, Institute for Materials, Institute for Robotics and Intelligent Machines, Georgia Institute of Technology, Atlanta, GA 30332, USA. *Corresponding author. Email: whyeo@gatech.edu

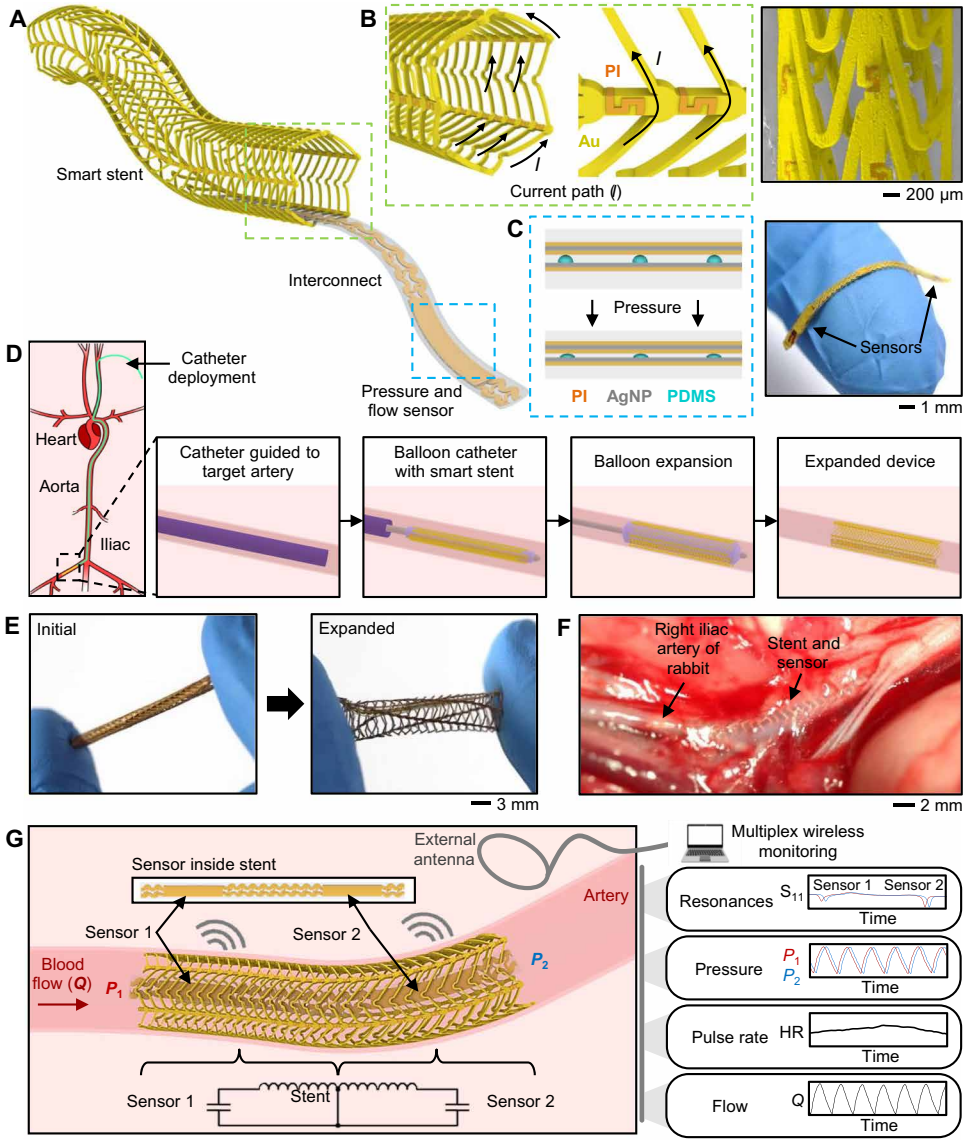

Fig. 1. Overview of a fully implantable, wireless vascular electronic system with printed sensors for wireless monitoring of hemodynamics. (**A**) Illustration of the implantable electronic components. (**B**) Inductive stent design using conductive Au loops and nonconductive polyimide (PI) connectors to achieve a current path resembling a solenoid (left) and an scanning electron microscopy (SEM) image of the stent (right). (**C**) Layers of the soft pressure sensor using a printed dielectric layer (left) and photo of index finger holding a simultaneous flow and pressure sensor (right). AgNP, silver nanoparticle; PDMS, polydimethylsiloxane. (**D**) Illustration of minimally invasive catheter deployment and balloon expansion of the wireless vascular stent. (**E**) Initial and expanded state of the sensor-integrated stent system. (**F**) Wireless stent system implanted in the right iliac artery of living rabbit. (**G**) Illustration of the wireless design and sensing scheme to simultaneously monitor pressure, heart rate (HR), and flow.

offers wireless monitoring of capacitive sensors while providing a reliable structure for implantation. The stent structure's main design and fabrication challenges offer sufficient wireless capabilities without deviating from typical stent mechanical properties. To accomplish this, a multimaterial stent uses conductive loops and nonconductive connectors to achieve a conductive pathway resembling a solenoid and serve as an inductive antenna (Fig. 1B). A scanning electron microscopy (SEM) image in Fig. 1B shows the fabricated stent. To unobtrusively sense hemodynamics, we laminate soft, low-profile pressure sensors on the inner surface of the stent. The capacitive sensors, shown in Fig. 1C on an index finger, use a structured dielectric layer for enhanced sensitivity and response time. The wireless device is compatible with catheter deployment, including delivery through a guide catheter and balloon expansion, as illustrated in Fig. 1D. The integrated stent and sensor shown in Fig. 1E have an initial diameter of 2 mm before expansion of up to 5 mm. Similar to conventional stents, the wireless device is readily adaptable for varying artery sizes. Owing to this adaptability and optimized mechanics, the device can be implanted via a minimally invasive catheter into a living rabbit's 1.93-mm-diameter iliac artery (Fig. 1F). For wireless sensing, the integrated stent and sensors form inductor-capacitor (LC) circuits with a resonant frequency dependent on pressure (Fig. 1G and section S1). While pressure monitoring requires only one sensor, placing a pressure sensor at

each end shares the stent and forms two LC circuits with distinct resonant frequencies. To detect both upstream and downstream pressures, the use of two sensors monitors a pressure gradient across the length of the stent, which allows for detecting flow rate changes. The resonant frequency of each circuit is wirelessly monitored with the S_{11} parameter via an external loop antenna and vector network analyzer (VNA). Overall, the wireless system enables real-time, simultaneous monitoring of pressure, pulse rate, and flow.

Fabrication and characterization of a wireless stent

Stent design and materials were evaluated to reconfigure a conventional stent as a wireless platform. A conventional stent is formed by loops and connectors of a single material (*26*). By removing connectors and organizing loops as a continuous path, a solenoid-like design is achieved, but this design is detrimental to stent mechanics and compatibility with balloon expansion (fig. S1) (*27*–*29*). Instead, here, an inductive stent design and fabrication process are developed to use conductive loops and nonconductive connectors, which prevents electrical shorting between adjacent loops. Fabrication steps are highlighted in Fig. 2A and rely on laser machining a cylindrical tube, which is a common stent fabrication strategy (details in Materials and Methods) (*26*). First, stainless steel tubing is laser-machined to remove material from the connector location before being dip-coated in polyimide (PI) to fill the connectors. After curing PI, the overall stent structure is laser-machined and then electropolished to remove impurities and smooth surfaces (fig. S2). To enhance the quality factor of the LC circuit, the resistance of the stent is decreased from 25 to 2 ohms by electroplating a 25-μm-thick layer of gold (Au) onto the steel surfaces (figs. S3 and S4). A 25-μm-thick layer of parylene, which has been previously shown to be biocompatible and hemocompatible, is deposited to insulate the stent and reinforce connectors (*30*–*32*). Figure 2B illustrates the stent design using conductive loops and nonconductive connectors to achieve a solenoid-like structure (details in fig. S1). The stent applied in this work uses 27 loops with a wire width of 120 μm and a length of 28 mm. The loop pattern can be varied to accommodate different diameters and inductances (fig. S5). While a variety of connector designs failed to endure laser machining, an "S" shape of PI with interlocking steel hooks is durable while adjacent insulating loops. Connectors failed when stretched because of insufficient adhesion between PI and steel, but the "S" shape reinforces the interface during stretching by the steel hooks compressing onto the center, the horizontal portion of the PI "S." An SEM image in Fig. 2C shows the inductive stent with enlarged views of the optimized connector (additional images in fig. S6). A 60-μm trace width of PI accommodates electroplating of the Au layer without electrically shorting across the connector. A cross-sectional image in Fig. 2D shows the multilayer coating of a stent strut without delamination (fig. S7). A collected set of photos and data in Fig. 2 (E and F) demonstrates balloon catheter expansion of the inductive stent from a diameter of 2 to 5 mm with pressure below 10 atm, which is comparable with conventional stents (*33*). The expansion increases inductance from 0.15 to 0.46 μH, which compares well with theoretical expectations, and minimally increases resistance as the loops deform (fig. S8). Stent photos in Fig. 2E show that the PI connectors enable uniform expansion and loop spacing. For comparison, removing the PI connectors causes distortion during expansion as a result of lowered axial stiffness (fig. S9) (*27*–*29*). While the stent uses 27 loops, the density and number of loops can be increased by reducing wire thickness, increasing inductance, and lowering expansion pressure (fig. S10). However, the addition of loops increases resistance because of a longer wire length, which diminishes wireless performance. A key benefit of reducing the strut thickness of the stainless steel base is to reduce the overall strut thickness of the wireless stent. Currently, the stent shows an average strut thickness of 190 μm. Future work will involve using a thinner stainless steel strut and minimizing coating thickness because thicker stents have shown lower endothelialization and higher risk of restenosis and complications (*34*–*37*). To demonstrate adaptability and widespread application for arteries, a smaller and thinner stent with an initial diameter below 1.5 mm and an expanded diameter up to 3 mm was fabricated with a strut (115 μm in thickness) and evaluated alongside the larger stent (fig. S11).

For wireless performance characterization, a loop reader antenna connected to a VNA recorded the S_{11} parameter of the expanded stent integrated with a printed capacitive sensor (fig. S12). The 5-mm-diameter stents with one pressure sensor and with two pressure sensors for flow sensing were tested, along with the 3-mm-diameter stent with one pressure sensor (fig. S13). Wireless readout distance of the stent in the air was measured in radial and axial directions and compared to an identically dimensioned solenoid inductor formed with copper (Cu) wire. Figure 2G compares the magnitude of the S_{11} parameter at resonance for the Cu coil and stent (details in fig. S14). The Cu coil achieved distances of 2 and 3 cm in the axial and radial directions, respectively, while the stent reached 1.5 and 2.0 cm. The distance was improved by tuning the external reader antenna with a capacitor, enabling radial distances of 5.5 cm for a large stent, 3 cm for a large stent with two sensors, and 3.5 cm for a small stent (Fig. 2H, details in fig. S15). Figure 2I shows the decrease in the signal magnitude of the frequency sweep at increasing distances. The wireless signal indicates a low-power transfer efficiency due to the small stent size and an unoptimized external reader system coupled with the device. Thus, future work will include applying for relevant works on inductive coupling, passive sensors, and wireless powering through biological tissues to develop and optimize external reader electronics and the overall wireless system consisting of the reader and implantable device to enhance efficiency, distance, and reliability (*38*–*40*). The external electronics will be improved with impedance-matching methods and an optimized frequency range based on stent dimensions, implant depth, and tissue absorption to improve device functionality and communication distance through biological tissues (*41*–*44*). Because implant locations in arteries may require bending of the stent, wireless performance was additionally observed when the stent is subject to bending. Wireless communication distance during bending of the stent to 30° notably affected the axial direction, while the radial direction remained unchanged (fig. S16). This occurs because of bending, causing degradation of axial alignment as axial distance increases while not affecting radial alignment. However, as the degree of bending increases, the wireless signal also degrades in the radial direction. Along with enhancing wireless performance, the multimaterial design notably improves stent mechanical properties compared to prior works (*45*). The key implantation criteria, including axial, bending, and radial stiffness, were measured and compared among four stents: an inductive stent with PI connectors, an inductive stent without connectors, an inductive stent with only steel, and a commercial stent (fig. S17) (*27*, *28*, *45*–*48*). As shown in Fig. 2J, the PI connectors are critical in

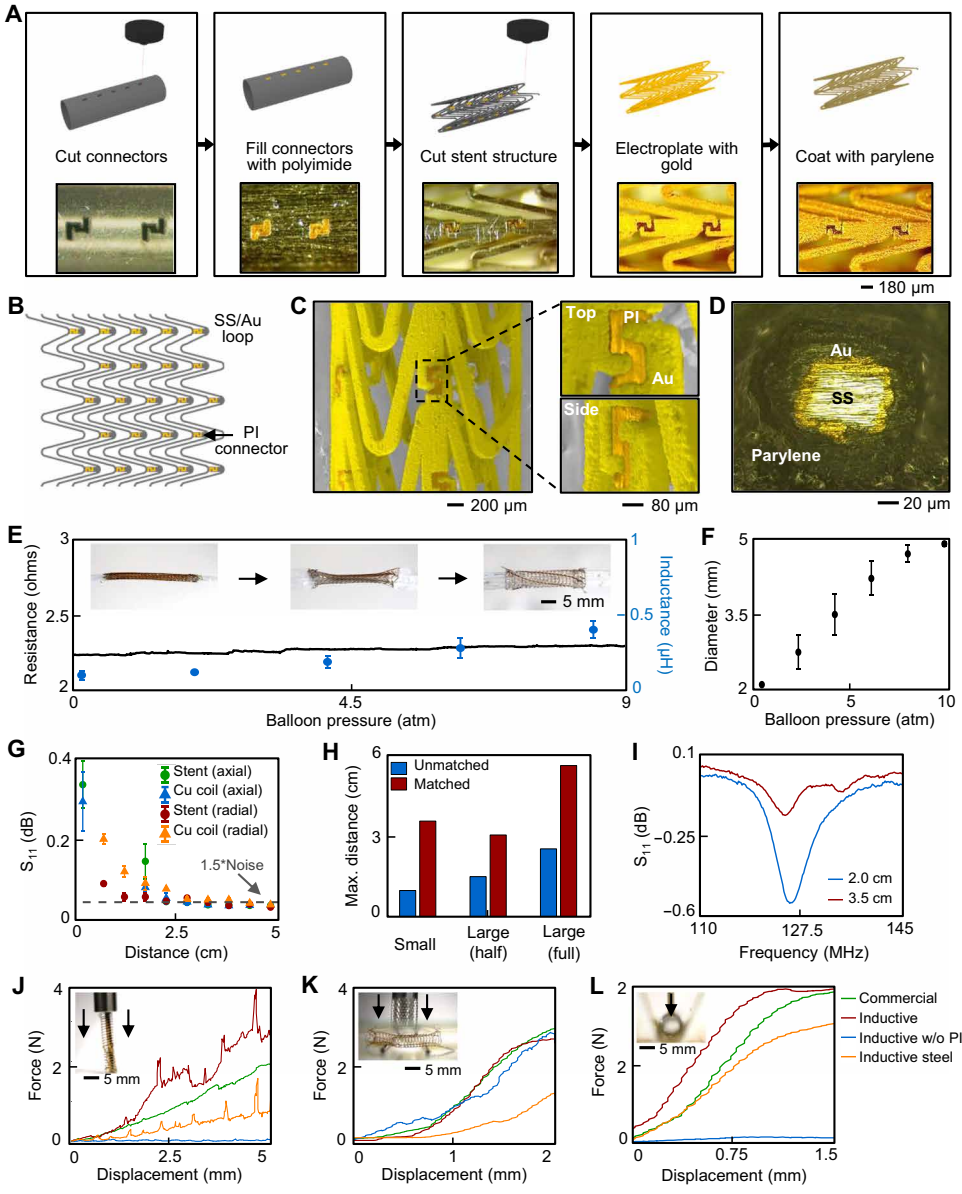

Fig. 2. Design, fabrication, and characterization of a wireless stent. (**A**) Illustration of fabrication steps for a multimaterial, inductive stent. (**B**) Layout of stent design using conductive Au loops and nonconductive PI connectors. (**C**) SEM images of stent structure showing PI connectors. Enlarged views of the PI connector showing separation of Au loops. (**D**) Cross-sectional image of a stent strut showing the layers of stainless steel (SS), Au, and parylene. (**E**) Balloon expansion of the wireless stent. Resistance shows a minimal increase while inductance increases. Photos show the progression of expansion on the balloon. (**F**) Increased stent diameter according to balloon pressure. (**G**) Magnitude of S_{11} parameter at the resonant frequency at different distances for the wireless stent and a Cu coil. A single-loop, unmatched antenna was used for wireless reading. Magnitude decreases with distance and becomes unreadable below the noise level. (**H**) Maximum wireless readout distance achieved by each stent with a single-loop antenna. Matching the antenna enhances readout distance. (**I**) Wireless frequency sweep of S_{11} parameter from a stent and sensor. Larger distances result in less pronounced resonant dips. (**J** to **L**) Measurement of axial stiffness (J), bending stiffness (K), and radial stiffness (L) of the wireless stent. Comparison is included with a commercial stent, a wireless stent without PI connectors, and an inductive stent design with stainless steel connectors.

providing axial stiffness comparable to a commercial stent. Although the brief increases in force result from connectors buckling, the overall stiffness of the inductive stent and commercial stent is similar. Bending stiffness was identical for all stents except the steel inductive stent because of the lack of Au coating, because increasing the thickness of the stent wires increases bending stiffness (Fig. 2K). Figure 2L shows similar radial stiffness of the inductive stent and commercial stent. The axial and radial collapses of the inductive stent without connectors indicate the importance of the PI connectors for structural integrity.

Design, fabrication, and characterization of a soft pressure sensor

The aerosol jet printing method was applied to enable a fully printed sensor by taking advantage of its rapid fabrication process compatible with a wide range of ink viscosities from 1 to 1000 cP. Figure 3A

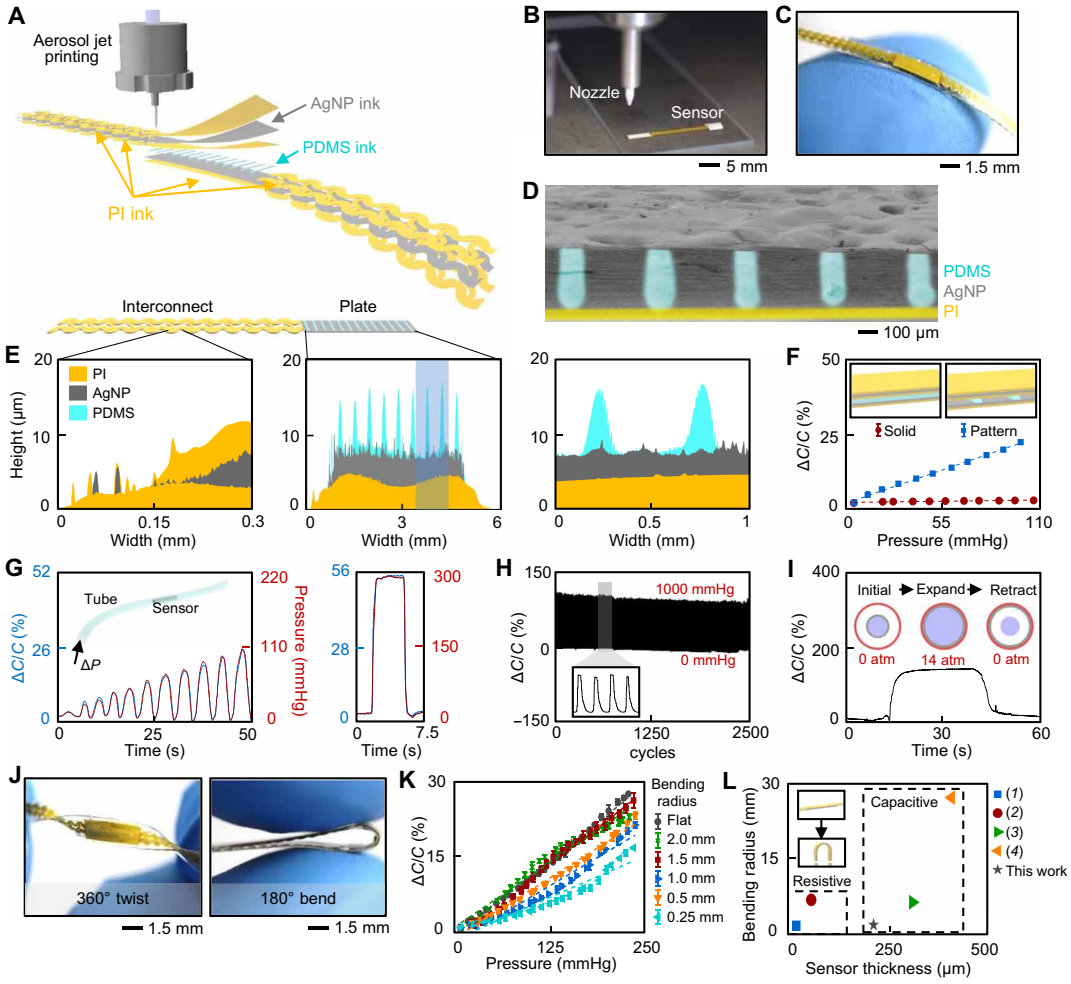

Fig. 3. Fabrication and characterization of soft pressure sensors. (**A**) Exploded view of sensor layers following sequential aerosol jet printing of PI, AgNP, and PDMS inks. The top and bottom electrodes are printed separately and laminated together. (**B**) Photo of aerosol jet nozzle for printing sensors. (**C**) Soft pressure sensor with interconnects held on a fingertip. (**D**) SEM image of the bottom electrode of a sensor consisting of a support PI layer, conductive AgNP layer, and dielectric PDMS layer. (**E**) Profile measurement of the interconnect (left), electrode (center), and enlarged view of the dielectric layer (right). (**F**) Pressure sensitivity is enhanced by using a dielectric layer of patterned PDMS lines compared to a solid thin film with similar thicknesses. (**G**) Sensor capacitance compares well with pressure waves over time (left) and sudden, large pressure changes (right). The sensor shows an immediate response to a 300-mmHg pressure increase and decrease. (**H**) Pressure cycling from 0 to 1000 mmHg for 2500 cycles showed minimal change in sensor performance. (**I**) Sensor response during balloon expansion with the wireless stent. (**J**) Demonstration of sensor twisting and bending without failure. (**K**) Sensor response to pressure when in a state of bending. Sensitivity stays constant at a 1.5-mm bending radius and maintains sensing capabilities beyond a 0.25-mm bending radius. (**L**) Comparison of the sensor to prior works on pressure sensing during bending. This work demonstrates pressure sensing at the lowest bending radius among capacitive pressure sensors and second-lowest among both sensor types.

illustrates the printed layers of PI, silver nanoparticles (AgNPs), and polydimethylsiloxane (PDMS) forming the pressure sensor with stretchable interconnects (details in Materials and Methods and fig. S18). The top and bottom electrodes are printed separately on the same substrate via a nozzle, as shown in Fig. 3B (movies S1 and S2). Following printing, the two layers are transferred and laminated together in elastomer, and the completed sensor is shown in Fig. 3C. PDMS encapsulation is used in this work because of the known hemocompatibility, which may be enhanced with surface modifications; future work will investigate other encapsulation materials (*49*, *50*). Ink and printing parameters were optimized to achieve a thin and durable sensor (table S1). A structured dielectric layer is printed with PDMS on the bottom electrode, as shown by the colored SEM image in Fig. 3D (movie S3). Following prior reports of molding PDMS microstructures to enhance pressure sensitivity, here, printing replaces molding to achieve rapid fabrication with fewer processes and direct PDMS patterning. Interconnect thickness is less than 12 μm, while the bottom electrode and the dielectric layer are less than 16 μm thick (Fig. 3E). The printed PDMS structures show uniformity and could be continuously printed on numerous sensors. Printing speed and the number of passes can be controlled to adjust the height and width of PDMS traces (fig. S19).

The dielectric layer of printed PDMS lines offers notably higher pressure sensitivity compared to a solid film, as shown in Fig. 3F, and achieves an average sensitivity of 0.013 kPa^{-1}. The improvement stems from the PDMS structures having space to deform under pressure. Capacitance values are shown as capacitance change divided by baseline capacitance ($\Delta C/C_0$). Typical baseline capacitances were 3 to 6 pF. The capacitive sensors indicated impacts of stray capacitance during wired tests, but these effects were not

observed once wires were removed and sensors were integrated with the wireless stent. A variety of PDMS patterns were printed, but the manual assembly of thin electrode results indicated similar sensitivities (fig. S20). All sensor results shown use printed PDMS lines with 525-μm centerline spacing. Future work will further optimize the printed PDMS structures. The sensor detects continuous pressure changes and displays an immediate response time even at high pressures (Fig. 2G). A solid dielectric layer slows response time and lowers sensitivity (fig. S20). The sensors display durability to cyclic pressure varied from 0 to 1000 mmHg, which is over 5× larger than artery pressures (Fig. 3H). In addition, it is critical for the sensor to withstand the pressure exerted onto a stent during balloon expansion. Figure 3I shows the sensor capacitance during stent deployment with a balloon pressure maintained at 14 atm for 30 s, which exceeds the typical time and pressure required to expand the inductive stent. Sensor capacitance increases and quickly decreases with a 3.5% baseline change after 60 s. The thin printed layers embedded in the elastomer offer a highly flexible sensor capable of twisting and bending without failure (Fig. 3J). The sensor conforms to bending radii smaller than 0.5 mm and recovers baseline capacitance (fig. S21). While prior pressure sensors offered flexible formats, many show sensitivity losses or are not demonstrated to sense pressure in a bending state (table S2) (*51*–*61*). By using thin active sensor layers and disconnected PDMS microstructures as the dielectric layer, the pressure sensor conforms to a bending radius of 1.5 mm without loss of sensitivity (Fig. 3K; details in fig. S22). Pressure sensing is demonstrated to a 0.25-mm bending radius, which is 20× smaller than prior capacitive pressure sensors and the second smallest among resistive pressure sensors (table S2) (*51*–*60*). Figure 3L shows a comparison to existing sensors, including both resistive and capacitive types. The larger thickness in this work compared to the resistive sensors results from the elastomer encapsulation.

Demonstration of a wireless device in an artery model

For implantation, the sensor is integrated within the stent and connected at each end to complete the LC circuit before crimping onto a balloon catheter and advancing through a guide catheter (Fig. 4A). The narrow sensor allows for attachment along the length of the stent to avoid excessive deformation of the sensor during stent expansion (fig. S23). The low-profile system is expanded into a silicone artery connected to a pulsatile pump to create physiological conditions (Fig. 4B, details in fig. S24). The stent and sensor were validated through wired monitoring of capacitance and wireless monitoring of resonant frequency, as illustrated in Fig. 4C. Figure 4D shows wired monitoring of sensor capacitance closely following the pulsatile pressure. A variety of pressures, flow rates, and pulse rates were applied to the sensor (fig. S25). During sensing, the low-profile form of the sensor avoids flow noise interferences despite large flow rate changes from 0 to 1000 ml min^{-1} (Fig. 4E). Wireless monitoring is achieved by continuously measuring the S_{11} parameter of the device with an external loop antenna and VNA. Figure 4F shows frequency sweeps of a device in the artery model at different pressures during pulsatile flow. Baseline resonant frequencies of devices in the artery model ranged from 70 to 110 MHz, depending on stent inductance and sensor capacitance. Continuous collection of frequency sweeps enables real-time monitoring of arterial pressure, as demonstrated in Fig. 4G. Owing to the fast response time of the pressure sensors, the device wirelessly detects the average, minimum, and maximum values of each pulsatile pressure waveform (Fig. 4H). Measurements in static air pressures demonstrated a wireless resolution as low as 5 mmHg, along with detection of sudden and large pressure changes (figs. S26 to S28). In the artery model, the wireless system monitored changes in system pressure, flow rate, and pulse rate, along with sudden, abnormal changes (figs. S29 to S31). With real-time pressure monitoring, pulse rates are simultaneously monitored by evaluating the recorded pulsatile wave frequency (fig. S30). Figure 4I compares pulse rates calculated using wireless device signals and using wired signals from a commercial pressure sensor.

Fitting the stent with two pressure sensors enables monitoring of flow rate changes in an artery (fig. S32). Each pressure sensor is located at the stent ends to detect a pressure gradient across the length of the stent. By electrically connecting the pressure sensors together at the center of the stent, the stent is split into two inductors and allows for monitoring two distinct resonant frequencies (72 and 105 MHz) to determine a pressure gradient (Fig. 4J, details in fig. S32). Figure 4K shows different flow rates, the average pressure gradient, and amplitude measured by the wireless device, which is similar to commercial pressure sensors. The difference in linearity may arise from the delay between wirelessly measuring the two sensors, wireless resolution, minor pressure changes within the stent, and the obtrusive attachment of commercial sensors to the artery. The increased difference at lower flow rates is expected to be caused by the increasingly smaller pressure gradient and a need for more precise calibration at lower pressures. However, the wireless system provided similar pressure values and captured flow changes, which indicates the ability to estimate flow rate and physiological changes, such as restenosis. Wireless performance when operated in blood and tissue was characterized. When operated in blood, the conductivity of blood dampens the inductive stent signal. While a thick parylene coating decreases this effect, operation in a saline concentration matching the conductivity of blood dampens the wireless signal, as shown in Fig. 4L (*24*). As a result, the readout distances are approximately halved when operating in a saline and through tissue surroundings (Fig. 4M, details in fig. S33). The distance of 5.5 cm in air and 3.5 cm in saline is an improvement over existing stent-based devices, which have been demonstrated up to 3 cm in air and 1 cm in the blood (Table 1) (*21*). Figure 4N shows the maximum 3-cm readout distance achieved through both saline and tissue for the 5-mm-diameter stent. Table 1 compares device performance with previously reported implantable arterial sensors (*9*, *17*, *18*, *21*–*23*). Compared to prior works, the presented device offers more comprehensive sensing of normal artery hemodynamics at the best readout distances while maintaining a low profile and demonstrates the most thorough in vivo catheter implantation for stent-based devices. It should be noted that prior work, showing longer communication distance, requires complete implantation by using a stent graft to fix itself in the aorta and only measures aneurysm sac pressure, not normal artery hemodynamics (*18*).

In vivo study of device implantation via a catheter

An in vivo rabbit study was performed to demonstrate catheter deployment. For implantation, a small inductive stent with an initial diameter below 1.5 mm and an expanded diameter up to 3.0 mm was used (Fig. 5A). An expanded device is shown in Fig. 5B with an enlarged view of the stent and a further miniaturized printed pressure sensor (fig. S34). In prior works on vascular sensors delivered by catheter, in vivo studies have been limited to minimal catheter

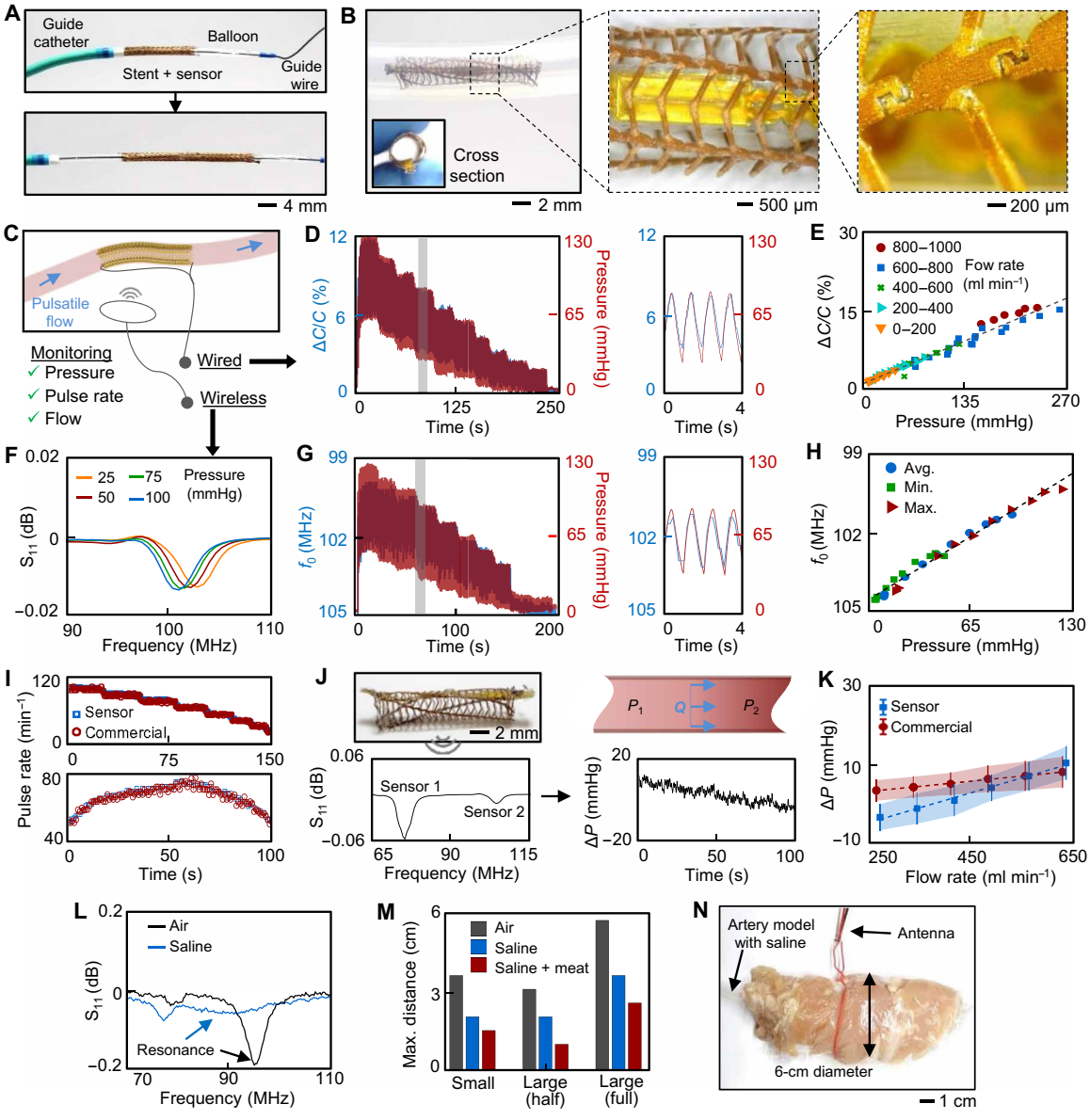

Fig. 4. Demonstration of wireless sensing of pressure, pulse, and flow. (**A**) Photo of wireless sensing system advancing through a guide catheter. (**B**) Expanded stent and sensor in artery model. Inset shows a cross section of the low-profile electronics. Enlarged views show the expanded stent structure and PI connectors. (**C**) Schematic of wired and wireless sensing methods in artery model. (**D**) Sensor capacitance during pulsatile flow in artery model with an enlarged view of pressure waveform. (**E**) Summary of wired sensor response during various flow rate levels. Capacitance increases linearly with pressure, indicating that flow has a minimal effect. (**F**) Wireless resonant frequency sweeps at different pressures. The resonant frequency decreases with increasing pressure. (**G**) Wireless pressure sensing in artery model with an enlarged view of the pulsatile wave. (**H**) Summary of wireless pressure sensing of average, maximum, and minimum pressures during pulsatile flow. (**I**) Pulse rate detection during two flow conditions. The wireless sensor detects a similar pulse rate to a commercial pressure sensor. (**J**) Wireless stent integrated with dual pressure sensor for monitoring of flow. The two sensors provide monitoring of two resonant frequencies, enabling real-time pressure gradient (ΔP) monitoring. (**K**) Summary of wireless flow monitoring comparing the pressure gradients monitored by the wireless sensor and commercial sensors. (**L**) Wireless signal from the device when operated in air and saline. The conductive surrounding lowers the wireless signal quality. (**M**) Wireless readout distances in air, saline, and saline plus tissue. (**N**) Photo of external antenna and artery model embedded in meat at maximum readout distance.

advancement, failed implantations, and the use of surgical grafts (*21*, *22*, *24*, *25*). Here, the wireless device was guided from a vascular sheath insertion site in the left carotid artery, over the aortic arch, through the abdominal aorta, and into the right iliac artery (Fig. 5C). This route is the most extensive implant demonstration via catheter for existing stent-based devices (Table 1). The pathway highlights the ability of the wireless device to advance through narrow and curved arteries with an aorta diameter of 4.5 mm and a right iliac artery diameter of 1.93 mm (fig. S35 and movie S4). Figure 5D shows fluoroscopy images during expansion and after catheter removal in the right iliac artery (fig. S36 and movie S5). Figure 5E shows photos of the implanted device in the right iliac artery following the in vivo study. In addition, a second wireless device was able to be guided around a sharp turn and into the left renal artery with a

Table 1. Performance comparison of implantable, wireless arterial sensors and systems.

Reference	Device type	Sensing parameter	Wireless distance (cm)		Wireless strategy	Device size (mm)	In vivo implantation
			Air	Blood			
This work	Soft, stretchable sensor	Pressure, pulse, and flow (artery hemodynamics)	5.5*	3.5	Inductive coupling	5 (*d*) 0.3 (*t*)	Catheter (Access: common carotid; implant: right iliac artery)
(*21*)	Rigid sensor	Pressure only	3	1	Inductive coupling	5 (*d*) 0.3† (*t*)	Vascular graft‡
(*22*)	Rigid sensor and memory modules	Temperature and flow	–§		radiofrequency	6 (*d*) 0.21 (*t*)	Catheter‖ (Access: common carotid; implant: common carotid)
(*17*)	Cuff-type sensor	Pulse¶	–		Inductive coupling	5 (*w*) 0.16# (*t*)	Suture**
(*23*)	Flexible sensor	Pressure only	0.8	–	Inductive coupling	3 (*d*) 0.15†† (*t*)	–
(*18*)	Planar sensor (required stent graft)	Pressure and pulse (aneurysm sac only)	>20‡‡ (complete implantation)		Inductive coupling	11 (*d*) 0.3 (*t*)	Stent graft and catheter (Access: femoral; implant: aorta)
(*9*)	Sensor package	Pressure and pulse	–§§		Inductive coupling	3.4 (*w*) 2 (*t*)	Catheter (Access: femoral; implant: pulmonary)

*Distance decreases to 3.0 cm for flow sensing. †Thickness estimated by combining stent and sensor thicknesses. ‡Device was implanted in graft, followed by attachment of graft. §Wireless signal magnitude measured from 1 to 5 cm but does not indicate what magnitude is sufficient. ‖Device was implanted with a wired connection. ¶Device was used to measure pulse rate and distinguish between flow and no-flow conditions. #Overall thickness determined by adding thicknesses of reported layers. **Device was wrapped around the artery and sutured to surrounding tissue. ††Thickness of sensor without a stent. ‡‡Device required complete implantation, not freestanding or self-supported like other devices. §§Distance is not reported, but the CardioMEMS HF system has been implanted in human trials.

diameter of 1.53 mm, indicating the potential for sensing in highly narrow arteries (fig. S37). Following the in vivo study, the right iliac artery was harvested to confirm the functionality of the implanted sensor (fig. S38). Future in vivo studies will monitor endothelial formation, restenosis, and long-term stability of the device. Figure 5F shows wireless signals from the stent before implantation, 2 hours after removal, and 3 months after removal. The resonance signals in Fig. 5F differ from the prior signals shown in Fig. 4F because of stent size differences. Signals shown in Fig. 4F were collected with a stent expanded to a 5-mm diameter, while signals in Fig. 5F were collected with a stent expanded to a 2-mm diameter. The smaller stent diameter causes a decrease in inductance and an increase in resonant frequency. In addition, variations in sensor base capacitance shift the frequency range of devices. Using a laminating press to more uniformly seal sensors will improve the consistency of the devices. The shift in resonant frequency from 175 to 135 MHz due to expansion compares well with theoretical calculations (Fig. 5G). For the implanted device, sensor capacitance and initial stent inductance were 5.3 pF and 0.15 μH, respectively. On the basis of these parameters, the theoretical resonant frequency of the device before expansion is 178 MHz (section S1). Following expansion from a diameter of 1.5 to 2 mm, the stent inductance is expected to increase to 0.26 μH, which shifts the resonant frequency to 136 MHz. Similar to that observed in vivo, pressure changes were applied to the harvested device and artery to ensure pressure sensing functionality (fig. S39). Figure 5H indicates the implanted device's change in resonant frequency with low-pressure ranges.

DISCUSSION

We have reported a fully implantable, vascular electronic system consisting of a wireless stent platform and printed soft sensors for real-time sensing of arterial pressure, pulse rate, and flow. Design, materials, and fabrication strategies of the inductive stent are developed to enhance wireless capabilities while maintaining key aspects of conventional stents. The fully printed capacitive sensors with microstructured features enable a notable improvement in pressure sensing during bending due to the thin, flexible layers and patterned PDMS. The wireless device demonstrates multiplex sensing of hemodynamics at extended readout distances in an artery model. An in vivo rabbit study shows minimally invasive catheter implantation in narrow arteries. Future work will improve sensor encapsulation,

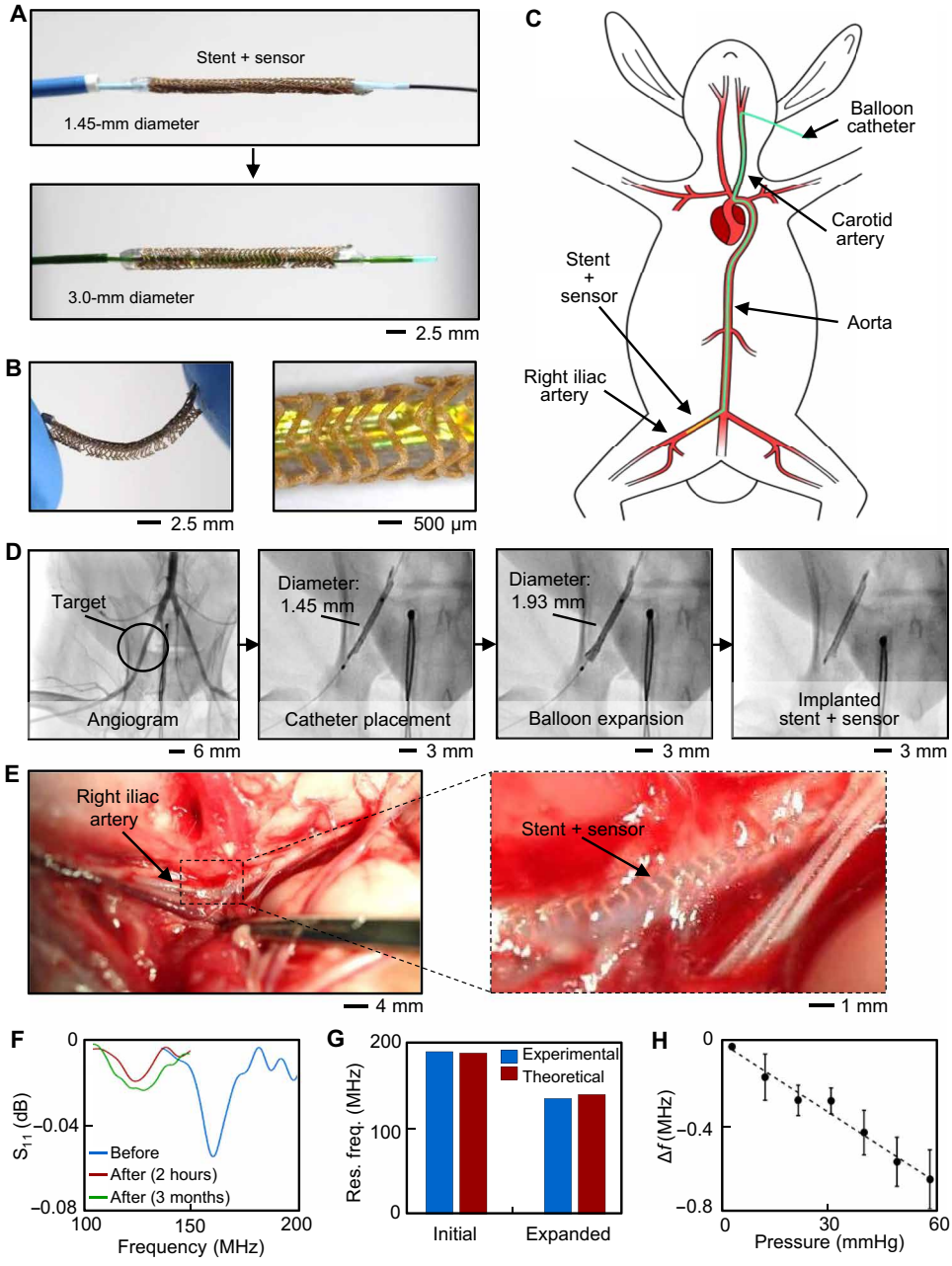

Fig. 5. In vivo study of implantation via a catheter. (**A**) Photo of 1.5-mm-diameter stent and sensor advanced through the guide catheter and expanded on a balloon. (**B**) Photos of expanded stent and sensor. (**C**) Schematic of in vivo catheter implantation in a rabbit where the wireless device is guided on a balloon catheter from the common carotid artery to the right iliac artery. (**D**) Fluoroscopy images showing the target site in the right iliac artery. Stent and sensor are guided to the right iliac artery followed by expansion and removal of the catheter. (**E**) Images of stent and sensor implanted in the right iliac artery. (**F**) Wireless frequency sweeps of the implanted sensor before implantation and after removal. Signals show a minor change 3 months later. (**G**) Resonant frequency before and after expansion matches theoretical prediction. (**H**) The harvested device is wirelessly interrogated in an artery model and demonstrates pressure detection.

reduce stent strut and sensor thickness, and develop external reader electronics, which will be used for in vivo long-term studies of implanted sensor functionality, endothelial formation, and inflammation concerns. Overall, the reported advancements in electronic designs, materials, and system integration enable opportunities for implantable vascular electronic systems and comprehensive wireless monitoring of hemodynamics. The wireless implantable device platform is readily adaptable for a multitude of sensors to monitor more parameters, such as strain, temperature, and biomarkers, and would allow for disease-specific devices.

MATERIALS AND METHODS

Fabrication of inductive stents

The inductive stent was fabricated with a femtosecond laser (Optec) using a tubing cutting stage. Stainless steel tubing (Vita Needle)

with an outer diameter of 2.1 mm and a wall thickness of 76 μm was the first laser-machined using a 60% power, a speed of 3.6 mm s^{-1}, and five passes to form holes for the connectors. Following cutting, the tubing was sonicated in deionized (DI) water to remove debris and clean the machined surfaces. Electropolishing was performed for 45 s with a current of 0.6 A in the electropolishing solution (E972, ESMA). The polished tubing was then rinsed with DI water and dried. The tubing was then dip-coated in PI (HD MicroSystems, PI-2545) before curing at 240°C for 1 hour. Dip coating and curing were then completed a second time to ensure full coverage. Following PI coating, sanding the surfaces of the tubing removed excess PI. The tubing was then laser-machined at identical parameters to form the final stent structure. Sonication in DI water and electropolishing of the stent structure was performed with identical parameters to clean surfaces. Surface plating of a 20-μm-thick layer of Au was performed by electrodeposition using a three-electrode system with a reference electrode (commercial Ag/AgCl electrode), Pt counter electrode, and the electropolished stent as a working electrode. The electrodes were submerged into a bright electroless gold plating solution (Sigma-Aldrich), and cyclic voltammetry deposition was conducted via a potentiostat (Gamry 1010E). During the deposition, the temperature and pH of the plating solution were controlled at 55°C and 8, respectively. The potential was swept from −0.65 to −0.95 V versus the commercial Ag/AgCl electrode for 850 cycles at a scan rate of 0.05 V s^{-1}. The surface of the Au-deposited stents was thoroughly rinsed by DI water to remove chemical residues that are potentially active and harmful in the implant circumstance. Following electroplating, a 25-μm-thick layer of parylene was deposited onto the stent using a parylene coater (SCS Labcoter).

Stent characterization

Balloon expansion was performed with a 5-mm-diameter balloon catheter (Cook Advance 18LP PTA) and an inflator with a pressure gauge filled with DI water. Small stents with an initial diameter of 1.5 mm used a 2-mm-diameter balloon catheter (Cordis Savvy Long PTA). Inductance was measured using an inductance-capacitance-resistance (LCR) meter (B&K Precision 891), and resistance was measured using a multimeter (Keithley DMM7510). Wireless frequency sweeps of the S_{11} parameter were recorded with a VNA (Tektronix TTR506A) controlled by a custom MATLAB program to determine the resonant frequency. The resonant frequency was determined by locating the minimum of the S_{11} parameter after subtracting a baseline frequency sweep. Loop reader antennas were formed with a single loop of Cu wire and connected to the VNA for recording. For performance comparison between a stent and Cu coil, the Cu coil was created by wrapping Cu wire around plastic tubing with a diameter, number of turns, and length equal to the stent. Noise levels were measured at frequencies lower and higher than resonance. Readout distances were measured for inductive stents connected to printed pressure sensors. Axial readout distance was measured by recording frequency sweeps while increasing the axial distance between the stent and external reader antenna. Radial readout distance was measured by recording frequency sweeps with different reader antenna diameters and placing the stent at the center of the reader antenna. To improve readout distance, external reader antennas were tuned with discrete ceramic capacitors to the resonant frequency of the stent and sensor. Stent's mechanical stiffness was measured with a motorized vertical test stand (Mark-10 ESM303) and force gauge (Marl-10 M5-5). The stage was moved by a set displacement while recording force. All stent samples, including the commercial stent (Medtronic Visi-Pro), were expanded to 4.5 mm in diameter.

Fabrication of soft pressure sensors

An aerosol jet printing system (Optomec 200) was used to print sensor layers. First, a layer of polymethyl methacrylate (PMMA; MicroChem) was spin-coated on a glass slide at 3000 rpm for 30 s and cured at 180°C for 3 min. The support layer of PI was printed via the pneumatic atomizer with parameters in table S1. The PI ink was formed in a 3.5:1 mixture of PI to 1-methyl-2-pyrrolidinone (Sigma-Aldrich). The bottom layer of PI was then cured in an oven at 240°C for 1 hour. Following curing, the printed PI was plasma-treated for 1 min before printing AgNP ink (UTDOTS, AgNP40X) via the ultrasonic atomizer with parameters in table S1. The AgNP layer was sintered at 240°C for 1 hour. After sintering, a top layer of PI was printed and cured with identical parameters. Printing of PDMS (Sylgard 184, Dow Corning) with the pneumatic atomizer and parameters in table S1 was then performed on the bottom electrode area of the sensor. PDMS ink was formed with an 18:4 mixture of 10:1 (base to cure) PDMS and toluene (StarTex). Printed PDMS was cured at 100°C for 1 hour. Following printing, the glass slide was covered and placed in an acetone bath for at least 1 hour to dissolve the underlying PMMA layer. After removing from the acetone bath, the sensors were transferred and aligned with tweezers onto elastomer. For transferring, the bottom electrode was first placed onto the elastomer with the PDMS dielectric layer facing up. The top electrode was then aligned and stacked on top of the bottom electrode. A small amount of PDMS was applied and cured along the interconnects to keep the sensor layers in place on the elastomer substrate. To seal the sensors, a piece of elastomer substrate was cut and laminated over the electrode area. A small amount of PDMS was poured and cured along the edges and interconnects while applying pressure to the elastomer piece covering the electrodes. After curing, the assembled and sealed sensor was removed from the plastic dish. Cu wires were attached to the interconnects with silver paint for wired sensing. The sensor was attached inside the stent for wireless sensing and connected to each end of the stent and the center of the stent with silver paint. A small amount of PDMS was used to insulate the electrical connections and to provide additional attachment points along the length of the sensor.

Sensor characterization

Sensor capacitance was recorded with the LCR meter. Pressure response was characterized by placing the sensors in silicone tubing connected with a syringe. The pressure was applied by displacing the syringe, while a commercial sensor (Honeywell 26PCBFB6G) recorded pressure. Pressure sensing during a bending state was accomplished by bending the sensor around glass slides and taping the sensor at both ends away from the bending area. Glass slides with a thickness of 1.0 mm were stacked and used for bending radii between 0.5 and 2.0 mm. A bending radius of 0.25 mm was maintained by taping the sensor interconnects together without a spacer in between. The pressure was then applied by displacing the syringe. Cyclic tests were performed using the motorized vertical test stand attached with a force gauge. The vertical stage applied pressure onto a sensor, while the LCR meter recorded capacitance. Compatibility with balloon catheter expansion was validated by attaching the sensor inside a stent. The stent was then expanded against the wall of silicone tubing while recording capacitance.

Wireless sensing in an artery model

An artery model, with a wireless device expanded within, was formed with silicone tubing connected to a pulsatile pump (Harvard Apparatus). Valves were included upstream and downstream of the wireless device to modify system pressure, while the pump was used to modify pulse rate from 0 to 120 min^{-1} and stroke volume from 0 to 10 ml. The flow of both DI water and saline was used to characterize sensing. A commercial pressure sensor was located near the sensor and stent to record pressure simultaneously. Wired measurements used an LCR meter, while wireless measurements used a VNA. The antenna was placed around the silicone artery and aligned with the stent for wireless sensing. Pulse rate was calculated by determining the maximum and minimum values of the recorded pressure and capacitance waveform. The time difference between the two was determined and converted to a pulse rate. A pressure gradient was wirelessly measured by recording the resonant frequency of each pressure sensor simultaneously. Before testing in flow, the resonant frequency of each sensor was measured for static pressure. By using static pressures, a calibration curve of resonant frequency and pressure was created for each sensor. During wireless recording in flow, the resonant frequency of each sensor was converted to pressure by using its calibration curve. The pressure difference between the sensors was then determined at each time point by subtracting the two pressure values. The calculated pressure difference determined the average pressure gradient and amplitude of the pressure gradient. For comparison, two commercial pressure sensors were located at a distance equal to the wireless device's sensors. The pressure gradient between the two commercial sensors was recorded. The wireless device was characterized when implanted in saline and meat to replicate in vivo conditions of blood and tissue. A saline concentration of 0.08 M was used to match the conductivity to blood (*62*–*64*). The meat was wrapped around the artery model to the specified thickness and extended more than 4 cm away from the implanted stent in both directions along the axial length.

In vivo demonstration

A New Zealand white rabbit was used in accordance with the approved protocol (#GT69B, T3 Labs, Global Center for Medical Innovation). Under inhalant isoflurane anesthesia, a vascular sheath was placed in the left carotid artery. The animal was then heparinized to achieve an active clotting time over 250 s. The device was mounted on a balloon catheter (Cordis Savvy Long PTA) and advanced over a 0.46-mm (0.018-inch) guidewire with fluoroscopic visualization. The device was advanced from the left carotid artery, over the aortic arch, and through the abdominal aorta to reach the targeted right iliac artery. The device was expanded with a balloon catheter pressure of 10 atm before removal of the catheter. The animal was monitored during the study. In vivo wireless measurements were found to be unreliable because of the small artery size and distance between the implanted device and skin. Following the in vivo study, the right iliac artery was harvested and stored in 10% neutral buffered formalin. The harvested device was maintained in the right iliac artery and placed inside silicone tubing for wireless testing of pressure sensing. Wireless signals were recorded 2 hours after harvesting and 3 months after harvesting. Wireless signal noise was removed using a low-pass filter and a cubic-smoothing spline. The pressure was applied by displacing a syringe, while a commercial pressure sensor was simultaneously recorded. Wireless signals were collected with a loop antenna and VNA.

SUPPLEMENTARY MATERIALS

Supplementary material for this article is available at https://science.org/doi/10.1126/sciadv.abm1175

REFERENCES AND NOTES

1. World Health Organization, Cardiovascular disease fact sheet (2017).
2. S. S. Virani, A. Alonso, E. J. Benjamin, M. S. Bittencourt, C. W. Callaway, A. P. Carson, A. M. Chamberlain, A. R. Chang, S. Cheng, F. N. Delling, Heart disease and stroke statistics—2020 update: A report from the American Heart Association. *Circulation* **141**, e139–e596 (2020).
3. B. R. Kwak, M. Bäck, M.-L. Bochaton-Piallat, G. Caligiuri, M. J. Daemen, P. F. Davies, I. E. Hoefer, P. Holvoet, H. Jo, R. Krams, Biomechanical factors in atherosclerosis: Mechanisms and clinical implications. *Eur. Heart J.* **35**, 3013–3020 (2014).
4. T. Pereira, C. Correia, J. Cardoso, Novel methods for pulse wave velocity measurement. *J. Med. Biol. Eng.* **35**, 555–565 (2015).
5. M. E. H. Ong, C. H. L. Ng, K. Goh, N. Liu, Z. X. Koh, N. Shahidah, T. T. Zhang, S. Fook-Chong, Z. Lin, Prediction of cardiac arrest in critically ill patients presenting to the emergency department using a machine learning score incorporating heart rate variability compared with the modified early warning score. *Crit. Care* **16**, R108 (2012).
6. J.-L. Vincent, A. Rhodes, A. Perel, G. S. Martin, G. Della Rocca, B. Vallet, M. R. Pinsky, C. K. Hofer, J.-L. Teboul, W.-P. de Boode, Clinical review: Update on hemodynamic monitoring-a consensus of 16. *Crit. Care* **15**, 229 (2011).
7. R. A. Nishimura, B. A. Carabello, Hemodynamics in the cardiac catheterization laboratory of the 21st century. *Circulation* **125**, 2138–2150 (2012).
8. J. K. Schmier, K. L. Ong, G. C. Fonarow, Cost-effectiveness of remote cardiac monitoring with the cardiomems heart failure system. *Clin. Cardiol.* **40**, 430–436 (2017).
9. Abbot, CardioMEMS HF System Program Practice Guide (2019).
10. L. M. Raj, L. A. Saxon, Haemodynamic monitoring devices in heart failure: Maximising benefit with digitally enabled patient centric care. *Arrhythmia Electrophysiol. Rev.* **7**, 294–298 (2018).
11. L. Hubbert, J. Baranowski, B. Delshad, H. Ahn, Left atrial pressure monitoring with an implantable wireless pressure sensor after implantation of a left ventricular assist device. *ASAIO J.* **63**, e60–e65 (2017).
12. I. C. Santos, J. M. R. Tavares, in *TMSi-Sixth International Conference on Technology and Medical Sciences* (2010).
13. R. Herbert, H.-R. Lim, S. Park, J.-H. Kim, W.-H. Yeo, Recent advances in printing technologies of nanomaterials for implantable wireless systems in health monitoring and diagnosis. *Adv. Healthcare Mat.* **10**, 2100158 (2021).
14. H. R. Lim, H. S. Kim, R. Qazi, Y. T. Kwon, J. W. Jeong, W. H. Yeo, Advanced soft materials, sensor integrations, and applications of wearable flexible hybrid electronics in healthcare, energy, and environment. *Adv. Mater.* **32**, 1901924 (2020).
15. R. Herbert, S. Mishra, H. R. Lim, H. Yoo, W. H. Yeo, Fully printed, wireless, stretchable implantable biosystem toward Batteryless, real-time monitoring of cerebral aneurysm hemodynamics. *Adv. Sci.* **6**, 1901034 (2019).
16. Y. J. Hong, H. Jeong, K. W. Cho, N. Lu, D. H. Kim, Wearable and implantable devices for cardiovascular healthcare: From monitoring to therapy based on flexible and stretchable electronics. *Adv. Funct. Mater.* **29**, 1808247 (2019).
17. C. M. Boutry, L. Beker, Y. Kaizawa, C. Vassos, H. Tran, A. C. Hinckley, R. Pfattner, S. Niu, J. Li, J. Claverie, Biodegradable and flexible arterial-pulse sensor for the wireless monitoring of blood flow. *Nat. Biomed. Eng.* **3**, 47–57 (2019).
18. M. A. Fonseca, M. G. Allen, J. Kroh, J. White, in *Tech. Dig. Solid-State Sensor, Actuator, and Microsystems Workshop (Hilton Head 2006)* (Citeseer, 2006), pp. 37–42.
19. J. Vishnu, G. Manivasagam, Perspectives on smart stents with sensors: From conventional permanent to novel bioabsorbable smart stent technologies. *Med. Devices Sens.* **3**, e10116 (2020).
20. H. M. van Beusekom, P. W. Serruys, "Drug-eluting stent endothelium: presence or dysfunction," (American College of Cardiology Foundation, 2010).
21. X. Chen, B. Assadsangabi, Y. Hsiang, K. Takahata, Enabling angioplasty-ready "smart" stents to detect in-stent restenosis and occlusion. *Adv. Sci.* **5**, 1700560 (2018).
22. D. Son, J. Lee, D. J. Lee, R. Ghaffari, S. Yun, S. J. Kim, J. E. Lee, H. R. Cho, S. Yoon, S. Yang, Bioresorbable electronic stent integrated with therapeutic nanoparticles for endovascular diseases. *ACS Nano* **9**, 5937–5946 (2015).
23. J. Park, J.-K. Kim, D.-S. Kim, A. Shanmugasundaram, S. A. Park, S. Kang, S.-H. Kim, M. H. Jeong, D.-W. Lee, Wireless pressure sensor integrated with a 3D printed polymer stent for smart health monitoring. *Sens. Actuators B. Chem.* **280**, 201–209 (2019).
24. X. Chen, D. Brox, B. Assadsangabi, Y. Hsiang, K. Takahata, Intelligent telemetric stent for wireless monitoring of intravascular pressure and its in vivo testing. *Biomed. Microdevices* **16**, 745–759 (2014).
25. S. R. Green, R. S. Kwon, G. H. Elta, Y. B. Gianchandani, In vivo and in situ evaluation of a wireless magnetoelastic sensor array for plastic biliary stent monitoring. *Biomed. Microdevices* **15**, 509–517 (2013).

26. D. Stoeckel, C. Bonsignore, S. Duda, A survey of stent designs. *Minim. Invasive Ther. Allied Technol.* **11**, 137–147 (2002).
27. J. A. Ormiston, B. Webber, M. W. Webster, Stent longitudinal integrity: Bench insights into a clinical problem. *JACC Cardiovasc. Interv.* **4**, 1310–1317 (2011).
28. J. A. Ormiston, B. Webber, B. Ubod, J. White, M. W. Webster, Stent longitudinal strength assessed using point compression: Insights from a second-generation, clinically related bench test. *Circ. Cardiovasc. Interv.* **7**, 62–69 (2014).
29. R. Vijayvergiya, A. Gupta, Longitudinal stent deformation during coronary intervention: A report of three cases. *IHJ Cardiovascular Case Reports (CVCR)* **1**, 68–71 (2017).
30. B. A. Weisenberg, D. L. Mooradian, Hemocompatibility of materials used in microelectromechanical systems: Platelet adhesion and morphology in vitro. *J. Biomed. Mater. Res.* **60**, 283–291 (2002).
31. S. K. Yazdani, A. Sheehy, S. Pacetti, B. Rittlemeyer, F. D. Kolodgie, R. Virmani, Stent coating integrity of durable and biodegradable coated drug eluting stents. *J. Interv. Cardiol.* **29**, 483–490 (2016).
32. W.-C. Kuo, T.-C. Wu, C.-F. Wu, W.-C. Wang, Bioperformance analysis of parylene C coating for implanted nickel titanium alloy. *Mater. Today Commun.* **27**, 102306 (2021).
33. G. R. Douglas, A. S. Phani, J. Gagnon, Analyses and design of expansion mechanisms of balloon expandable vascular stents. *J. Biomech.* **47**, 1438–1446 (2014).
34. J. M. Jiménez, P. F. Davies, Hemodynamically driven stent strut design. *Ann. Biomed. Eng.* **37**, 1483–1494 (2009).
35. N. Foin, R. D. Lee, R. Torii, J. L. Guitierrez-Chico, A. Mattesini, S. Nijjer, S. Sen, R. Petraco, J. E. Davies, C. Di Mario, Impact of stent strut design in metallic stents and biodegradable scaffolds. *Int. J. Cardiol.* **177**, 800–808 (2014).
36. H. Hara, M. Nakamura, J. C. Palmaz, R. S. Schwartz, Role of stent design and coatings on restenosis and thrombosis. *Adv. Drug Deliv. Rev.* **58**, 377–386 (2006).
37. C. Briguori, C. Sarais, P. Pagnotta, F. Liistro, M. Montorfano, A. Chieffo, F. Sgura, N. Corvaja, R. Albiero, G. Stankovic, In-stent restenosis in small coronary arteries: impact of strut thickness. *J. Am. Coll. Cardiol.* **40**, 403–409 (2002).
38. P. T. Theilmann, P. M. Asbeck, An analytical model for inductively coupled implantable biomedical devices with ferrite rods. *IEEE Trans. Biomed. Circuits Syst.* **3**, 43–52 (2009).
39. L. Rindorf, L. Lading, O. Breinbjerg, in *SENSORS, 2008 IEEE* (IEEE, 2008), pp. 1611–1614.
40. A. Ibrahim, M. Kiani, A figure-of-merit for design and optimization of inductive power transmission links for millimeter-sized biomedical implants. *IEEE Trans. Biomed. Circuits Syst.* **10**, 1100–1111 (2016).
41. A. Ibrahim, M. Meng, M. Kiani, A comprehensive comparative study on inductive and ultrasonic wireless power transmission to biomedical implants. *IEEE Sens. J.* **18**, 3813–3826 (2018).
42. S. Stoecklin, A. Yousaf, T. Volk, L. Reindl, Efficient wireless powering of biomedical sensor systems for multichannel brain implants. *IEEE Trans. Instrum. Meas.* **65**, 754–764 (2016).
43. J. C. Lin, A new IEEE standard for safety levels with respect to human exposure to radio-frequency radiation. *IEEE Antennas Propag. Mag.* **48**, 157–159 (2006).
44. A. S. Poon, S. O'Driscoll, T. H. Meng, Optimal frequency for wireless power transmission into dispersive tissue. *IEEE Trans. Antennas Propag.* **58**, 1739–1750 (2010).
45. A. R. Mohammadi, M. S. M. Ali, D. Lappin, C. Schlosser, K. Takahata, Inductive antenna stent: Design, fabrication and characterization. *J. Micromech. Microeng.* **23**, 025015 (2013).
46. K. Schmitz, D. Behrend, P. Behrens, W. Schmidt, Comparative studies of different stent designs. *Prog. Biomed. Res.* **4**, 52–58 (1999).
47. T. Duerig, M. Wholey, A comparison of balloon-and self-expanding stents. *Minim. Invasive Ther. Allied Technol.* **11**, 173–178 (2002).
48. R. L. Noad, C. G. Hanratty, S. J. Walsh, Clinical impact of stent design. *Interv. Cardiol.* **9**, 89–93 (2014).
49. C. Howe, S. Mishra, Y.-S. Kim, Y. Chen, S.-H. Ye, W. R. Wagner, J.-W. Jeong, H.-S. Byun, J.-H. Kim, Y. Chun, Stretchable, implantable, nanostructured flow-diverter system for quantification of intra-aneurysmal hemodynamics. *ACS Nano* **12**, 8706–8716 (2018).
50. P. Xue, Q. Li, Y. Li, L. Sun, L. Zhang, Z. Xu, Y. Kang, Surface modification of poly (dimethylsiloxane) with polydopamine and hyaluronic acid to enhance hemocompatibility for potential applications in medical implants or devices. *ACS Appl. Mater. Interfaces* **9**, 33632–33644 (2017).
51. Y. Joo, J. Yoon, J. Ha, T. Kim, S. Lee, B. Lee, C. Pang, Y. Hong, Highly sensitive and bendable capacitive pressure sensor and its application to 1 V operation pressure-sensitive transistor. *Adv. Electron. Mater.* **3**, 1600455 (2017).
52. S. C. Mannsfeld, B. C. Tee, R. M. Stoltenberg, C. V. H. Chen, S. Barman, B. V. Muir, A. N. Sokolov, C. Reese, Z. Bao, Highly sensitive flexible pressure sensors with microstructured rubber dielectric layers. *Nat. Mater.* **9**, 859–864 (2010).
53. G. Schwartz, B. C.-K. Tee, J. Mei, A. L. Appleton, D. H. Kim, H. Wang, Z. Bao, Flexible polymer transistors with high pressure sensitivity for application in electronic skin and health monitoring. *Nat. Commun.* **4**, 1–8 (2013).
54. C. M. Boutry, A. Nguyen, Q. O. Lawal, A. Chortos, S. R.-Gagné, Z. Bao, A sensitive and biodegradable pressure sensor array for cardiovascular monitoring. *Adv. Mat.* **27**, 6954–6961 (2015).
55. C. M. Boutry, Y. Kaizawa, B. C. Schroeder, A. Chortos, A. Legrand, Z. Wang, J. Chang, P. Fox, Z. Bao, A stretchable and biodegradable strain and pressure sensor for orthopaedic application. *Nat. Electron.* **1**, 314–321 (2018).
56. Q. Lin, J. Huang, J. Yang, Y. Huang, Y. Zhang, Y. Wang, J. Zhang, Y. Wang, L. Yuan, M. Cai, Highly sensitive flexible iontronic pressure sensor for fingertip pulse monitoring. *Adv. Healthc. Mater.* **9**, 2001023 (2020).
57. S. Lee, A. Reuveny, J. Reeder, S. Lee, H. Jin, Q. Liu, T. Yokota, T. Sekitani, T. Isoyama, Y. Abe, A transparent bending-insensitive pressure sensor. *Nat. Nanotechnol.* **11**, 472–478 (2016).
58. S. J. K. O'Neill, H. Gong, N. Matsuhisa, S. Chen, H. Moon, H. C. Wu, X. Chen, X. Chen, Z. Bao, A carbon flower based flexible pressure sensor made from large-area coating. *Adv. Mater. Interfaces* **7**, 2000875 (2020).
59. N. Luo, Y. Huang, J. Liu, S. C. Chen, C. P. Wong, N. Zhao, Hollow-structured graphene–Silicone-composite-based piezoresistive sensors: Decoupled property tuning and bending reliability. *Adv. Mater.* **29**, 1702675 (2017).
60. H. B. Yao, J. Ge, C. F. Wang, X. Wang, W. Hu, Z. J. Zheng, Y. Ni, S. H. Yu, A flexible and highly pressure-sensitive graphene–polyurethane sponge based on fractured microstructure design. *Adv. Mater.* **25**, 6692–6698 (2013).
61. Y. Huang, X. Fan, S. C. Chen, N. Zhao, Emerging technologies of flexible pressure sensors: Materials, modeling, devices, and manufacturing. *Adv. Funct. Mater.* **29**, 1808509 (2019).
62. A. R. Mohammadi, K. Chen, M. S. M. Ali, K. Takahata, Radio aneurysm coils for noninvasive detection of cerebral embolization failures: A preliminary study. *Biosens. Bioelectron.* **30**, 300–305 (2011).
63. C. Balan, C. Balut, L. Gheorghe, C. Gheorghe, E. Gheorghiu, G. Ursu, Electrical and rheological properties of blood in simple shear flow. Part I: Experimental determination of blood permittivity and conductivity. *Clin. Hemorheol. Microcirc.* **30**, 359–364 (2004).
64. A. Peyman, C. Gabriel, E. Grant, Complex permittivity of sodium chloride solutions at microwave frequencies. *Bioelectromagnetics* **28**, 264–274 (2007).

Acknowledgments

Funding: We acknowledge the support of the American Heart Association (grant 19IPLOI34760577), and this work was partially supported by the National Institutes of Health (NIH) under award number (NIH R03EB028928). The content is solely the responsibility of the authors and does not necessarily represent the official views of the NIH. Electronic devices in this work were fabricated at the Institute for Electronics and Nanotechnology, a member of the National Nanotechnology Coordinated Infrastructure, which is supported by the National Science Foundation (grant ECCS-2025462). **Author contributions:** R.H. and W.-H.Y. designed the study. R.H., H.-R.L., and B.R. performed experiments and data analysis. R.H. performed in vivo study. R.H. and W.-H.Y. wrote the paper. **Competing interests:** R.H. and W.-H.Y. are the inventors for a pending U.S. patent application (no. 63/085,652) related to the work described here. The authors declare that they have no other competing interests. **Data and materials availability:** All data needed to evaluate the conclusions in the paper are present in the paper and/or the Supplementary Materials.

Submitted 31 August 2021
Accepted 29 March 2022
Published 11 May 2022
10.1126/sciadv.abm1175

Science Advances

Fully implantable wireless batteryless vascular electronics with printed soft sensors for multiplex sensing of hemodynamics

Robert HerbertHyo-Ryoung LimBruno RigoWoon-Hong Yeo

Sci. Adv., 8 (19), eabm1175. • DOI: 10.1126/sciadv.abm1175

Science Advances (ISSN) is published by the American Association for the Advancement of Science. 1200 New York Avenue NW, Washington, DC 20005. The title *Science Advances* is a registered trademark of AAAS.